






<b>Publication Year</b>	2022
<b>Acceptance in OA</b>	2025-02-04T15:32:46Z
<b>Title</b>	Relative Astrometry in an Annular Field
<b>Authors</b>	GAI, Mario, VECCHIATO, Alberto, RIVA, Alberto, Butkevich, A. G., BUSONERO, Deborah, Qi, Z., LATTANZI, Mario Gilberto
<b>Publisher's version (DOI)</b>	10.1088/1538-3873/ac50a1
<b>Handle</b>	<a href="http://hdl.handle.net/20.500.12386/35801">http://hdl.handle.net/20.500.12386/35801</a>
<b>Journal</b>	PUBLICATIONS OF THE ASTRONOMICAL SOCIETY OF THE PACIFIC
<b>Volume</b>	134



# Relative Astrometry in an Annular Field

M. Gai<sup>1,4</sup> , A. Vecchiato<sup>1</sup> , A. Riva<sup>1</sup>, A. G. Butkevich<sup>1,2</sup>, D. Busonero<sup>1</sup>, Z. Qi<sup>3</sup>, and M. G. Lattanzi<sup>1</sup> 

<sup>1</sup>INAF—Osservatorio Astrofisico di Torino via Osservatorio 20—I-10025 Pino Torinese (TO), Italy

<sup>2</sup>Pulkovo Observatory, Russian Academy of Sciences Pulkovskoye chaussee 65—Saint Petersburg 196140, Russia

<sup>3</sup>Shanghai Astronomical Observatory, Chinese Academy of Sciences 80 Nandan Rd.—Shanghai 200030, People's Republic of China

Received 2021 December 21; accepted 2022 January 31; published 2022 March 18

## Abstract

*Background.* Relative astrometry at or below the microarcsec level with a 1 m class space telescope has been repeatedly proposed as a tool for exo-planet detection and characterization, as well as for several topics at the forefront of Astrophysics and Fundamental Physics. *Aim.* This paper investigates the potential benefits of an instrument concept based on an annular field of view, as compared to a traditional focal plane imaging a contiguous area close to the telescope optical axis. *Method.* Basic aspects of relative astrometry are reviewed as a function of the distribution on the sky of reference stars brighter than  $G = 12$  mag (from Gaia EDR3). Statistics of field stars for targets down to  $G = 8$  mag is evaluated by analysis and simulation. *Results.* Observation efficiency benefits from prior knowledge on individual targets, since source model is improved with few measurements. Dedicated observations (10–20 hr) can constrain the orbital inclination of exoplanets to a few degrees. Observing strategy can be tailored to include a sample of stars, materialising the reference frame, sufficiently large to average down the residual catalog errors to the desired microarcsec level. For most targets, the annular field provides typically more reference stars, by a factor four to seven in our case, than the conventional field. The brightest reference stars for each target are up to 2 mag brighter. *Conclusions.* The proposed annular field telescope concept improves on observation flexibility and/or astrometric performance with respect to conventional designs. It appears therefore as an appealing contribution to optimization of future relative astrometry missions.

*Unified Astronomy Thesaurus concepts:* [Astronomical instrumentation \(799\)](#); [Space astrometry \(1541\)](#); [Astrometric exoplanet detection \(2130\)](#); [Space vehicle instruments \(1548\)](#)

## 1. Introduction

Astrometry from space bears the promise of achieving substantially photon- and diffraction-limited precision to measurement of celestial object positions (and related quantities: motion, parallax, separation, ...). Moreover, such precision may be achieved on either narrow or large angular separation among targets, providing the tools to achieve full-sky (global or absolute) measurements. The most advanced large scale implementation of such ideas is currently Gaia (Prusti et al. 2016), which has recently delivered its Early Data Release 3 (EDR3) (Gaia Collaboration et al. 2021), with remarkable astrometric quality (Lindegren et al. 2021), expected to further improve in future releases.

However, as any scientific progress is a stepping stone toward the next challenge, a number of other space missions have been, and will be, proposed to further advance our capability of understanding the universe by better measurements. These will be discussed in the following.

Photon-limited precision at the microarcsec (hereafter,  $\mu\text{as}$ ) level, or better, translates into comparable accuracy only at the expense of significant efforts in terms of instrument design and

calibration efforts, which also affects operation. Calibration of the optical response is obviously alleviated in case of a nearly ideal instrument, with small deviation from the diffraction limited Point-Spread Function (PSF). Advanced metrology concepts, improving on the knowledge of instrument response, have also been investigated (Zhai et al. 2011).

The science case for high precision, narrow angle astrometry has been presented e.g., in the context of the proposed space mission Theia (Malbet et al. 2021). Exo-planetary science missions based on astrometry have also been investigated in other approaches (Bendek et al. 2018; Tuthill et al. 2018; Shao et al. 2019). Also observatory class missions like the Roman Space Telescope (RST) (Croft 2021) bear the potential for impressive results, in that case with lower angular precision, but on much fainter extra-galactic objects. We retain as reference most of the goals of the above concepts, but we introduce a significant modification in the instrument and operation implementation concept, which we expect to be beneficial with respect to calibration and control of systematic errors related to variation of the telescope optical response.

The recently proposed idea (Riva et al. 2020) of a Ring Astrometric Field Telescope for Exoplanets and Relativity (RAFTER), reviewed in Section 3, is characterized by a field of

<sup>4</sup> Author to whom any correspondence should be addressed.

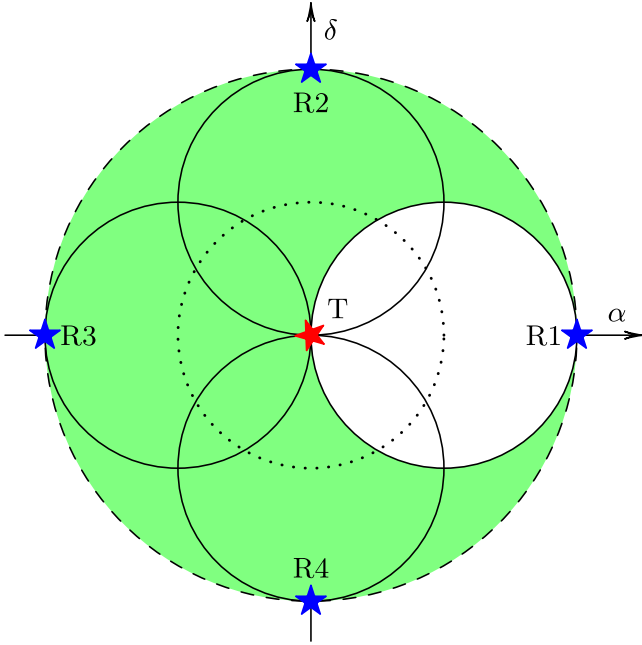


**Figure 1.** Field ( $2^\circ$  radius, shaded) accessible to the target star  $T$  (center) by pointing the telescope along the dotted circle ( $1^\circ$  radius): reference stars  $R1$ ,  $R2$ ,  $R3$  and  $R4$  are shown at  $\pm 2^\circ$  on either coordinate.

view, and related detection system, deployed over a circular strip centered around the projection of the optical axis. Also, circular symmetry is preserved throughout the optical system, thus ensuring circular symmetry of the instrument response, as described in Section 3.1.

The annular field of RAFTER (radius  $\theta$ , width  $\delta\theta$ ) allows simultaneous observation of source pairs at a significantly larger angular separation (up to  $2\theta$ ) than in case of a conventional round geometry detector, which concentrates the same area  $2\pi\theta\delta\theta$  within radius  $\sim\sqrt{2\theta\delta\theta}$ . The principle is depicted in Figure 1, with  $\theta = 1^\circ$  and  $\delta\theta \ll \theta$ : the target star  $T$  is located at the center, and four reference stars ( $R1$ ,  $R2$ ,  $R3$  and  $R4$ ) are placed at extreme positions on either axes. The target and any object in the whole shaded area (dashed circle) can be observed simultaneously, by setting the telescope optical axis in suitable points on the dotted circle, i.e., pivoting the field of view around the target.

Such instrument concept allows selection of the actual field of view close to a given target with some liberty, according to performance optimization criteria. In particular, we may select a region around the science target including the brightest accessible reference star; other *ad hoc* criteria may be adopted when convenient, e.g., maximizing the number of field stars. Some such options are investigated in our study and detailed in Section 5.1.

This framework appears to be efficient toward implementation of robust narrow angle astrometry, exploiting available

references (the Gaia catalog) and/or strengthening it with additional observations to improve on individual source parameters.

In Section 2 we briefly review some of the compelling science topics supporting a high precision relative astrometry mission; in Section 3 the RAFTER instrument concept is recalled and some relevant aspects of operation with an annular field are outlined. In Section 4 the practical case of relative astrometry on a specific exoplanetary system is expounded in some detail. In Section 5 we derive the main statistical implications of annular field observation around the brightest stars in the sky. Finally, in Section 6, we draw our conclusions.

## 2. Overview of the Science Case

As shown in Section 3, RAFTER is a suggested technical implementation of a relative astrometry mission similar e.g., to Theia. The science cases of these two missions, thus, share a lot of similarities, differences emerging especially in consideration of the different observing strategies allowed by the annular field of view of RAFTER versus the concentrated one of Theia.

Limiting ourselves to a short review of the possible scientific applications of this mission concept, RAFTER has the possibility to contribute to the detection and orbit characterization of Earth- to Superearth-sized exoplanets, as well as to several General Relativity and Cosmology related issues. For example, high precision astrometry on selected stellar samples will be able to probe the distribution (shape, radial profile, lumpiness) of the Dark Matter (DM) halo of the Milky Way, and possibly M31, by determination of the dynamics of dwarf spheroidal galaxies (dSph), globular clusters and halo streams within the Local Group as mapped by a significant fraction of their brightest stars, and precise masses, distances and proper motions to binary stars with black hole (BH) and neutron star (NS) companions will also be obtained from  $\mu\text{as}$  level measurement of their orbits. This includes the prototype of this class, Cygnus X-1 (Miller-Jones et al. 2021).

Another potential contribution is in the field of solar system dynamics. In the solar system there exist  $\sim 100$  objects whose maximum visual magnitude is  $V \leq 10$  or brighter, for which RAFTER can provide Micro- and sub-microarcsecond astrometry. Most of them are asteroids of the main belt, whose ephemerides can be improved by these measurements, at least for the vast majority of them that was not visited by a dedicated space probe, with potential implications in the field of solar system dynamics. Moreover, high-precision determination of the orbits of the Galilean satellites can be combined with data from the Juno or the planned ESA JUICE mission to obtain improved constraints on the internal structure of Jupiter.

More details on a few selected aspects of the scientific case are given in the following subsections.

### 2.1. Exoplanets: State of the Art

The current exoplanet count is at level 5000. Specifically, as of 2021 November 1st, NASA Exoplanet Archive ([exoplanetarchive.ipac.caltech.edu](http://exoplanetarchive.ipac.caltech.edu)) lists 4566 confirmed planets (along with 4663 TESS transit candidates), while the less restrictive Extrasolar Planets Encyclopaedia ([exoplanet.eu](http://exoplanet.eu)) lists 4868 confirmed in 3597 systems. Most such planets have been detected through photometric transit and radial velocity measurements ( $\sim 71\%$  and  $20\%$ , respectively), while the others have been discovered using astrometry, transits timing, microlensing and other methods. Perryman (2018) offers comprehensive discussion of various techniques employed to detect exoplanets.

The systems with confirmed planets evidence a rich diversity of objects. For example, planetary masses range over six orders of magnitude, extending from a  $70 M_J$  brown dwarf (Casewell et al. 2020) down to a  $0.02 M_{\oplus}$  super Mercury (Rappaport et al. 2012). A remark concerning terminology is due: although brown dwarfs are classified as substellar objects, we do not differentiate between them and planets for brevity. This should raise no ambiguity in the text.

The current exoplanetary census contains 43 confirmed Earth-like planets, i.e., with masses ranging from  $0.6$  to  $2.3 M_{\oplus}$ . Most of them (36) have been detected from primary transit searches, while microlensing observations and radial velocity surveys revealed five and one planet, respectively. The discovery of the last planet in the list, KOI-55 c, is remarkable: its existence was inferred from the brightness pulsation of its host star (Charpinet et al. 2011).

The large number of detected exoplanets encourage the belief that many, if not all, stars host planetary systems. The major detection techniques, i.e., photometric transit and radial velocity, however, suffer from a strong selection effect. Transits are observable only in case of edge-on systems, when our line-of-sight is almost parallel to the orbital plane. The probability that orientation of a planet orbit is favorable for transit detection is determined by the ratio of the stellar radius  $R_{\star}$  to the size of planet orbit  $a_p$  (Borucki & Summers 1984; Perryman 2018):

$$p \simeq 0.005 \left( \frac{R_{\star}}{R_{\oplus}} \right) \left( \frac{a_p}{1 \text{ au}} \right)^{-1}. \quad (1)$$

The geometric probability depends on neither star distance nor planet size. For example, for a Sun twin ( $R_{\star} = R_{\odot}$ ), the probability is  $0.5\%$  for the Earth and  $0.1\%$  for Jupiter. For a solar type star, the probability is above  $1\%$  if  $a_p \lesssim 0.5 \text{ au}$ , while for a AOV host star with  $2.5 R_{\odot}$  a  $1\%$ -probability zone extends to  $0.8 \text{ au}$ .

Although conditions are more relaxed for radial velocity measurements, discovery efficiency is still maximal for edge-on orbit orientation. The variation of star velocity due to orbital motion becomes less detectable as orbit inclination and/or companion mass decrease ( $m \sin i$  effect).

Thus, only a small fraction of exoplanets can be addressed by the two most widely used detection techniques. Face-on orbits, when orbital plane is nearly perpendicular to the line of sight, are mostly undetectable by either transit or radial velocity methods. In contrast, astrometric measurements are not subject to the above mentioned geometric limitations and can detect reflex motion of the star in any orbit configuration.

We address astrometric exoplanet detection in more detail in Section 4. Like radial velocities, astrometric measurements are more sensitive to massive components. There is a marked difference in the way that observed effects depend on star distance. Both eclipse depth and radial velocity amplitude are distance-independent, though the related photometric accuracy, of course, is affected. As a geometric effect, however, the astrometric signature scales inversely with distance (see Equation (6) below). This naturally favors usage of astrometry to search for planets orbiting stars in the solar vicinity.

It is worth mentioning that each detection technique has its own advantages and disadvantages; simultaneous exploitation of different techniques offers the best chances for determination of various parameters of components and host stars. The multi-planet system  $\pi$  Mensæ, for which combination of spectroscopic observations carried out at the ESO's Very Large Telescope, photometric transits observed by TESS, and Gaia astrometric data provided the 3D architecture of its planetary orbits (Damasso et al. 2020), gives a good examples of such synergy.

Moreover, the combination of new and previous astrometric measurements can provide new insight and better parameter determination on several cases, e.g., resolving binaries with stellar or substellar companions by proper motion anomaly (Kervella et al. 2019).

### 2.2. General Relativity and Cosmology-related Experiments

One interesting possibility is that of searching for possible deviations from Newtonian dynamics in near Wide Binaries (WBs). This opportunity was explored in a recent paper by Banik & Kroupa (2019) that simulated the feasibility of detecting MOND-like astrometric signals in the orbit of Proxima Centauri around  $\alpha$  Centauri A and B. This work concluded that a successful detection requires about  $T = 10 \text{ yr}$  of observations with  $f = 3$  observations per year at an accuracy of  $\sigma \leq 0.33 \mu\text{as}$ , which is within the reach of the proposed Theia mission (Malbet et al. 2021), and thus of the RAFTER mission as it will be explained below. This duration can be reduced by increasing the cadence of the observations, as a result of a  $S/N \propto T^{5/2} f^{1/2}$ . Moreover, the annular field of view gives the RAFTER concept a better opportunity with respect to Theia for this specific science case. As mentioned in the cited paper, in fact, basically this experiment aims at measuring the relative acceleration between Proxima and  $\alpha$  Centauri. In the

case of Theia, whose field of view of  $0.5^\circ$  is smaller than the angular separation of  $2.18^\circ$  between these two stars, this goal can be reached only by building an accurate reference frame with a sufficient number of stable reference stars, whereas the  $\sim 1^\circ$  radius of the annular field of RAFTER allows, in principle, to measure directly such a relative acceleration.

The actual number of existing stellar-mass BHs is an unsolved question that can potentially affect our understanding of galactic evolution in the early universe (Wheeler & Johnson 2011). Moreover, the hypothesis that DM may be constituted by Primordial Black Holes (PBH) in the solar-mass range had been thoroughly investigated in the past and rejected by several observational constraints (see e.g., Jedamzik (2020) for a list of relevant references). In the same paper, however, the author casts doubts on these conclusions, arguing that these limits rely on the correctness of the PBH binary semimajor and eccentricity distribution, and that it can evolve to be made consistent with present data. One technique that can be used to detect these PBH is the astrometric microlensing, and RAFTER can open up new possibilities in this respect.

Microlensing happens when a massive object passes in between an observer and a background source of light, aligned exactly or almost exactly with them. In such a case, the light of the background source is deflected by the massive objects, which behaves like a lens whose optical effects, unlike normal lenses, are produced by its gravity pull. The background object can appear magnified and distorted at the observer's position.

This phenomenon stems from the well-known effect of light deflection, stating that a mass  $M$  shifts the observed position of a light source from its nominal position on an amount given by  $\alpha = 4GM/(c^2b)$ , where  $b$  is the impact parameter of the null geodesic connecting the source and the observer.

In the microlensing phenomenon, the original source is seen very close to the deflecting object by the observer, and as a consequence it is split into two distinct images, each presenting two main effects (Boden et al. 1998): a photometric effect in which the intensities of the two images are magnified, and an astrometric effect in which the background source is displaced from its nominal position by a small angle.

Quantitatively, the appearance of microlensing is governed by the lens mass and by the three distances between the source (s), the lens (l) and the observer (o). The impact parameter can be written as function of these quantities as  $b = d_{so}/(d_{sl}d_{lo})$ , and in the literature the angular displacement is often defined in units of the so-called angular Einstein radius

$$\theta_E = \sqrt{\frac{4GM}{c^2} \frac{d_{sl}}{d_{so}d_{lo}}} = \sqrt{\frac{4GM}{c^2} (d_{lo}^{-1} - d_{so}^{-1})}, \quad (2)$$

which represents the displacement when the three objects are perfectly aligned.

By defining the angular separation  $u$  between the lens and the source in units of  $\theta_E$ , the intensity of each image writes

$$A_{1,2} = \frac{u^2 + 2}{2u\sqrt{u^2 + 4}} \pm \frac{1}{2}; \quad (3)$$

since typically  $\theta_E \sim 1$  mas, for on-ground observations the image separation is below the resolution of the observing instrument, and the lensed source appears as a single object with intensity

$$A = A_1 + A_2 = \frac{u^2 + 2}{u\sqrt{u^2 + 4}}. \quad (4)$$

Similarly, for what regards the astrometric effect, the background source is displaced from its nominal position by an angle

$$\delta\theta = \frac{u}{u^2 + 2}\theta_E. \quad (5)$$

While microlensing events are relatively easy to detect with photometric measurements, its astrometric displacement is very difficult to measure, at least from the ground. On the other side, estimating the mass of the lens exploiting photometric measurements only is extremely difficult when the lens is a single objects, as in the case of a PBH.

Without entering into much detail, which the interested reader can find in Lu et al. (2016), it is sufficient to note that Equation (2) shows how the mass of the lens can be inferred by the knowledge of  $\theta_E$ . This quantity is directly related to the astrometric displacement, while, for single-object lenses, its estimation with photometric measurements only requires a nearly direct passage of the source over the lens.

The potential of microlensing for determining trigonometric parallaxes is also worth mentioning. As recently demonstrated by Rybicki et al. (2022), an intensive photometric follow-up of the microlensing event Gaia19bld allowed not only to compute the lens mass but also to derive its distance with a 10% accuracy. Operating in continuous observing mode, RAFTER can provide dense coverage of brightness variation during a microlensing event to find lens properties from photometric data, in addition to the astrometric effect described by Equations (2) to (5). Thus, RAFTER is potentially capable of using both photometric and astrometric distance determination methods, giving another good example of synergy between different observational techniques.

RAFTER can help to shed light on the problem of the existence and composition of DM also by helping to improve the sample of Hypervelocity stars (HVS). These objects are considered a promising powerful probe to infer information about the gravitational potential of the Milky Way in the galactic halo, namely the Dark-Matter-dominated region of our galaxy according to the concordance  $\Lambda$ CDM model.

A recently published paper (Contigiani et al. 2019) proposes a new technique able to put stringent constraints on the

gravitational potential of the Milky Way using the mass, position, and velocity distributions of the HVSs. In this paper the authors put their method to test under an ideal but realistic scenario based on the predicted results of the ESA Gaia astrometric mission, showing that 200 HVSs are able to provide estimations of the Navarro–Frenk–White potential parameters with sub-percent uncertainties.

The accuracy of these constraints depends on the size of the HVSs sample, and previous works of the same authors (Marchetti et al. 2017, 2018) showed that suitable HVS candidates can be identified with neural network techniques that depend solely on the astrometric parameters. The reliability of the identification, however, depends on the uncertainties on parallaxes and proper motions, a requirement that conveniently matches the RAFTER purpose of prolonging and improving the astrometric accuracy of the Gaia catalog.

In addition to the improvement on the HVSs sample, RAFTER can contribute to the DM investigation also by observations of halo WBs. Their small binding energy, in fact, makes them very susceptible to external perturbations (passing stars, molecular clouds, spiral arms, large-scale tides, and massive objects in general), which allows them to be used to study the medium in which they are immersed. Therefore, halo wide-binaries can be used to study fine details of the gravitational potential of that Galactic component, placing relevant constraints on the nature of Dark matter (Yoo et al. 2004; Quinn et al. 2010). Given their extremely long periods (and large semimajor axis) their confirmation as a true gravitational pair requires very high-precision relative astrometry, currently available for only relatively small samples (see e.g., Gould & Chanamé 2004; Coronado et al. 2018; Tian et al. 2020). Gaia DR3 will surely provide many new candidates (usually through common proper-motion, supplemented with high-precision ground-based radial velocities), but an instrument like RAFTER could be used to follow-up on them, and confirm/discard their true binary nature.

### 3. The RAFTER Concept

The telescope, recently described in the literature (Riva et al. 2020), is designed with the goal of achieving good imaging quality, and above all good astrometric performance over a comparably large field of view. The latter requirement is implemented through the prescription of preserving circular symmetry at each stage of the optical system, down to and including the focal plane. The annular field thus provide invariance of the image characteristics along the azimuthal coordinate (at fixed angular radius from the optical axis), and smooth variation in the radial direction. This ensures that systematic errors related to instrument optical response are minimized, at least along one coordinate. The RST also uses part of the annular corrected field of its optical design (Pasquale et al. 2014) in its Wide Field Imager, whose  $3 \times 6$  chips are arranged in a semi-lunar (“smile”) layout.

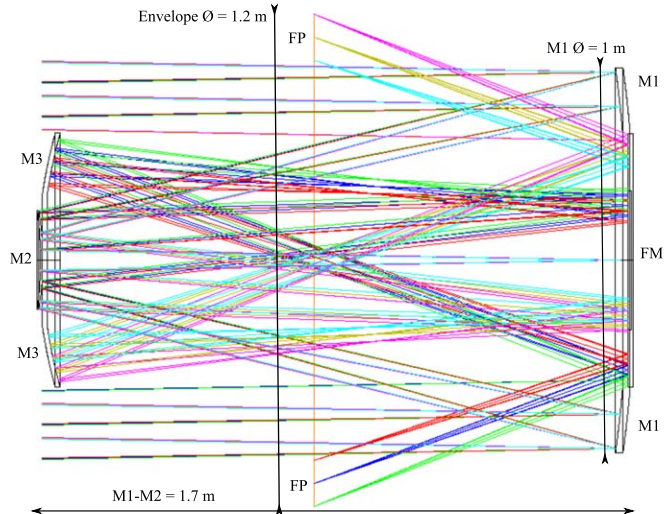


**Figure 2.** The RAFTER telescope layout. The focal plane (FP) is deployed on a ring surrounding the input beam (baffling not shown).

The proposed design achieves sub- $\mu$ as systematic error on azimuth, even with moderate perturbations to the nominal configuration, and  $<2$  mas distortion over the radial range  $[0^\circ.9, 1^\circ.1]$ , easily modeled. The diffraction limited field ( $>1.25$  square deg) is partially populated by 66  $4k$  detectors on a  $4'$  wide ring (0.26 square deg).

#### 3.1. Optical System main Characteristics

The RAFTER design is derived from a classical Three Mirror Anastigmat (Korsch 1977), optimized with the explicit goal of exploiting a full ring within the annular corrected field. The telescope layout is shown in Figure 2, in its CCD-compatible version with effective focal length  $EFL = 30$  m. The peculiarity is that the secondary (M2) and tertiary (M3) mirrors are placed within each other, as well as the primary (M1) and a flat folding mirror (FM). The input pupil and all mirrors are annular, i.e., they use only a circular region. The flat FM has the double function of feeding the optical path from M2 to M3, and from M3 to the focal plane (FP), a ring of CCD detectors around the telescope main tube. The system is therefore highly symmetric and very compact: 1.7 m length, 1.2 m diameter. Optical design characteristics, including indications on robustness against perturbations, have been published (Riva et al. 2020).

#### 3.2. A Strawman Mission: Key Elements

The actual design of payload and satellite is beyond the scope of the current study, mostly focused on the instrument concept and related operation options. A few aspects are proposed, in order to define the framework for the subsequent discussion.

RAFTER is assumed to be operated on a pointed satellite, aimed at comparably long observations of selected targets to achieve high precision, rather than a scanning mission covering the whole celestial sphere (or large fractions thereof), and necessarily devoting little time to individual sources.

The 1 m class telescope is consistent with the main payload of a medium class mission, driving satellite and operation design. Additional payloads are not considered herein, but such option will be an obvious concern of the supporting agencies throughout early mission definition phases. The operating orbit can be selected with some freedom after finalisation of the science case priorities; GEO and L2 are obvious possibilities suggested by previous missions. The mission lifetime is assumed to be of order of five years. Longer duration, obviously impacting costs, is beneficial to an astrometric mission, allowing observation of more targets and/or improved determination of their dynamical parameters, above all for long period orbits.

At any given time, the sky area accessible will be limited by attitude consideration, including the need to avoid the Sun on the payload, and to feed the solar array providing the power supply. Besides, this results in a geometric constraint on observations, so that most targets may be observed a few times a year, e.g., in epochs grouped over about a semester.

We assume a typical observation time of order of one hour. If the fractional time required to switch between subsequent targets is  $\sim 10\%$ , it may be possible to operate order of 20 observations per day, for a total of  $\sim 7000$  observations per year. Since several sources will require two or more observations per year, an acceptable number of individual science targets is on the order of few thousand.

Careful definition of the science case will therefore be required to maximize the mission output, trading off the competing requirements of large samples and fine sampling over the mission lifetime. In practice, a few targets, requiring higher precision and/or time resolution, may be observed several times, and others less frequently.

### 3.3. High Cadence Observations

Broadband observation of bright sources with a sizeable telescope results in fast detector saturation. A long integration, required to achieve high precision thanks to a correspondingly high photon budget, must therefore be split into many shorter elementary exposures, with the data co-added either on board or on ground. This also provides a valuable high frequency information on pointing stability, which may be taken advantage of by the on-board attitude and orbit control system. Multiple exposure astrometry on bright stars is also discussed in a separate paper (Gai et al., submitted to PASP).

Full detector readout on a short timescale would be impractical, but, since bright sources are few and usually wide apart, we can set windows around them for selective readout,

discarding less interesting regions. On-board detection, required for proper management of readout windows, is routinely used on Gaia.

The detector readout is assumed to be performed on a pixel period of  $5 \mu\text{s}$ , not very challenging with respect to modern science instrumentation. Full frame readout on single-output  $4k \times 4k$  devices requires about 80 s, thus window readout is required for all chips imaging sources brighter than  $G \simeq 15.5$  mag. Several large windows (e.g.,  $44 \times 44$  pixels) can be read with source magnitude  $G \gtrsim 8$  mag; then, size and number of windows must be reduced. A single, small window ( $10 \times 10$  pixels) per chip may allow imaging for stars as bright as  $G \simeq 2.5$  mag.

### 3.4. Calibration Hints

The capability of an annular field with radius  $\theta$  to observe at the same time a selected target and any source within angular distance  $2\theta$  was anticipated in the Introduction and illustrated in Figure 1.

By rotation around the optical axis, the same pair of objects can be observed repeatedly in different detector positions, thus contributing to both measurement statistics and calibration. Subsequent estimates of the pair separation can be expected to differ by amounts related to the instrument response variation over the field, assuming that the observation is short with respect to the natural timescale of variation of both payload and astrophysical sources. Repeated observations on longer time-scales will remove the degeneration between correlated instrument variations, and uncorrelated evolution of different sources.

The goal precision of RAFTER is below the error level expected on individual sources in the final Gaia catalog, but comparable to the intrinsic precision of the underlying Gaia reference frame. Therefore, statistics on a sufficiently large sample will average down the resulting collective error to adequate levels.

Pairwise observation of several nearby objects, not simultaneously fitting within the annular field of view, allows measurement of the target against different reference sources and with different sampling geometry with respect to the instrument radial and azimuthal coordinates. The example shown in Figure 3 is a set of three targets, labeled  $A$ ,  $B$  and  $C$ , observed pairwise by application of small pointing offsets among subsequent positions  $C_A$ ,  $C_B$  and  $C_C$  of the optical axis.

### 3.5. Relative Astrometry: The Local Reference Frame

Each target is located with respect to the available population of field stars, materialising a local representation of the global Gaia reference frame. Since the goal measurement precision is below the  $1 \mu\text{as}$  range, we may wonder whether the Gaia precision is adequate to the task.

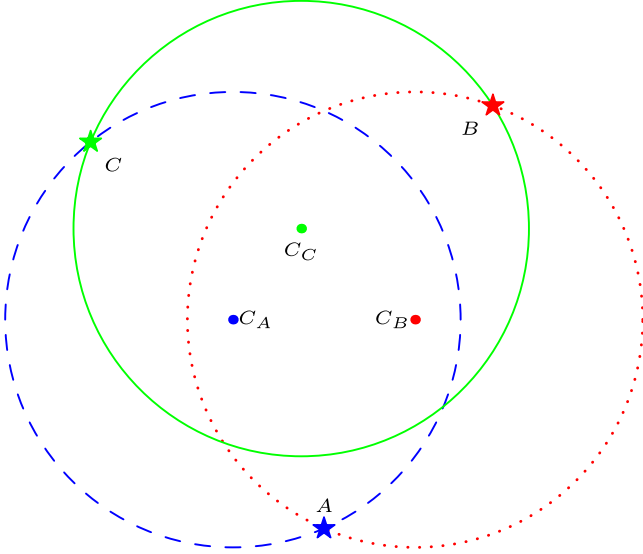


**Figure 3.** Example of pairwise observation of three targets  $A$ ,  $B$  and  $C$ , using three pointing offset positions.

Although a complete answer for each science case should be substantiated by a thorough, dedicated investigation, we address briefly some of the main aspects involved. Simple conceptual considerations and simulations seem to provide encouraging hints with respect to the feasibility of our ambitious precision goal.

The catalog uncertainty on reference objects affects the evaluation of any target’s dynamics in different ways:

1. Individual position errors induce an offset on the photocenter, constant over the mission lifetime.
2. Individual proper motion errors induce a continuous photocenter drift, appearing as a contribution to the linear motion of the target.
3. Individual parallax errors generate a reflex parallax term on the target.

The first term is inessential for most purposes, and the second term does not affect the measurement of the target’s astrometric wobbling. The third contribution is potentially more critical, since it induces an apparent oscillation on the target’s linear motion, which may be erroneously interpreted as the astrometric effect of an orbiting companion.

Of course, astrometric measurements are intrinsically affected by troubles in the detection of orbital periods close to one year, because it is difficult to disentangle them from the modulation applied by the Earth’s motion around the Sun. The difficulty is somewhat mitigated by geometry, since the target’s orbit will not usually be similar to the Earth’s orbit projection involved in the parallax method; however, the superposition might make the estimate more prone to errors. The degeneration may be reduced by a long sequence of astrometric observations, and sometimes broken by introduction of additional astrophysical information.

### 3.6. Cosmic Noise

A concern for high precision astrometry is the intrinsic astrometric variability of reference stars around a selected target, induced by a number of reasons: photospheric activity, starspots, undetected companions, and so on. While the issue is quite relevant and deserves *ad hoc* studies for any specific application and target, we can remark that the above assessment on the number of field stars provides some encouraging element.

Each source may have its own amplitude and timescale of variation; however, they can hardly be expected to have the same direction and phase. The mitigation of catalog errors by averaging them over a sufficiently large sample of field stars (as in Section 5.5) is a sort of “brute force” statistical approach. This may be expected to work as well in levelling out the individual astrometric fluctuations from the photocenter estimate used as a reference to evaluate the target motion.

## 4. Astrometry Optimization on Exoplanets

Astrometric information is used in exoplanetary studies to solve two tasks: discovery of new objects and characterization of known systems. Both these tasks are based on examining effect of exoplanets, or, more generally, unseen companions, on their host stars. Detection of planets relies on analysis of deviation of apparent path of the host from the single stars. Size of this effect is conveniently described by the so-called astrometric signature (Butkevich 2018; Perryman 2018; Ranalli et al. 2018; Sozzetti et al. 2014)

$$v = 3 \mu\text{as} \times \left( \frac{M_p}{M_\oplus} \right) \left( \frac{M_\star}{M_\odot} \right)^{-1} \left( \frac{a_p}{1 \text{ au}} \right) \left( \frac{d}{1 \text{ pc}} \right)^{-1}, \quad (6)$$

where  $d$  is the distance,  $a_p = (M_\star/M_p)a_\star$  is the semimajor axis of the planet orbit,  $M_\star$  and  $M_p$  the host star and planet mass, respectively;  $a_\star$  is the size of the stellar orbit around the system’s barycenter. For Earth-type planets, astrometric signatures are at the sub- $\mu\text{as}$  level. For example, if a  $1 M_\oplus$  planet orbits a Solar-mass star at  $a_p = 1 \text{ au}$ , the signature ranges from 0.3 to 0.03  $\mu\text{as}$  for stars in the volume between  $d = 10$  and 100 pc. In contrast, massive planets have more prominent effect on their host stars. For instance, the impact of a Jupiter ( $a_p = 5 \text{ au}$ ) amounts to  $\simeq 1 \text{ mas}$  for a  $0.5 M_\odot$  M dwarf at 10 au. However, planets at large  $a_p$  need relatively long measurements for reliable detection.

### 4.1. Mission Related Constraints

Simulations showed that astrometry is most efficient in discovering exoplanets with orbital period not exceeding the duration of observations (Perryman et al. 2014; Sozzetti et al. 2014). In view of the anticipated mission lifetime of 5 yr, therefore, we restrict our analysis to planets with orbital period  $P \lesssim 5 \text{ yr}$ . Making use the Kepler’s third law, we obtain the

corresponding constraint on the detectable orbit size

$$a_p \lesssim a_{\max} \simeq 3 \text{ au} \times \left( \frac{M_\star}{M_\odot} \right)^{1/2}. \quad (7)$$

This condition means that for upper main sequence host stars ( $M_\star \simeq 10 M_\odot$ ) the semimajor axis of planet orbit is limited to  $\lesssim 10$  au, while it should be below  $\simeq 1$  au for lower main sequence stars ( $M_\star \simeq 0.1 M_\odot$ ).

Astrometric discovery of exoplanets crucially depends on the signal-to-noise ratio  $v/\sigma$ , with  $\sigma$  being the astrometric accuracy. We adopt the ordinary three-sigma rule, that is, we assume  $v \geq 3\sigma$  in the following. This criterion, together with the above condition for the maximum orbit size, enables us to establish a lower limit to the planet mass. Rearranging Equation (6) and applying Equation (7), we find that

$$M_p \gtrsim M_{\min} \simeq M_\oplus \left( \frac{\sigma}{3 \mu\text{as}} \right) \left( \frac{M_\star}{M_\odot} \right)^{1/2} \left( \frac{d}{1 \text{ pc}} \right). \quad (8)$$

This equation is convenient for estimation of the minimum mass of astrometrically detectable planet in terms of accuracy, host star mass and distance.

Our simulations (Section 5.4) show that a precision level of few  $\sigma = 0.1 \mu\text{as}$  is achievable with the RAFTER design on one hour exposures on very bright stars ( $G \lesssim 4$  mag); the value  $\sigma = 0.2 \mu\text{as}$  is used below, in our assessment of planets that can be discovered. Table 4 gives predictions for the accuracy, including the precision level expected on nearby reference stars materialising the reference frame. However, these estimations are affected by operations and other error sources, which are preliminarily addressed in Sections 5.4 to 5.6. Therefore, the value of  $0.2 \mu\text{as}$  is to be taken as a representative estimate of foreseen astrometric performance.

Figure 4 illustrates the minimum detectable planet mass versus distance for three different host star masses: solar ( $1 M_\odot$ ), low- ( $0.1 M_\odot$ ) and upper- ( $10 M_\odot$ ) main sequence. This plot shows that an Earth-mass planet can be detected up to  $d = 15$  pc for solar-mass stars, while for  $0.1 M_\odot$  stars, e.g., M6 dwarfs, the Earth discovery limit is at  $\simeq 47$  pc. For a  $1 M_\odot$  host star, the lower detectable planet mass runs from  $0.7$  to  $7 M_\oplus$  as distance goes from 10 to 100 pc. For low-mass stars, the corresponding lower limit ranges from  $0.2$  to  $2 M_\oplus$ .

For massive stars, the astrometric effect from an Earth orbiting a  $10 M_\odot$  star remains undetectable by RAFTER even at 10 pc. This result lends itself to a straightforward interpretation. For such a star, the minimum detectable orbit size from Equation (7) is  $a_p \lesssim 9.5$  au. The corresponding astrometric signature of an Earth-mass planet at 10 pc is  $\simeq 0.3 \mu\text{as}$ , i.e., a detection level of  $1.5\sigma$ , well below the adopted  $3\sigma$ -threshold. The minimum detectable planet mass runs from 2 to  $20 M_\oplus$ , over distances ranging from 10 to 100 pc, for a  $M = 10 M_\odot$  host star. Equation (8) suggests that, at 10 pc, the astrometric motion caused by an Earth-mass planet is

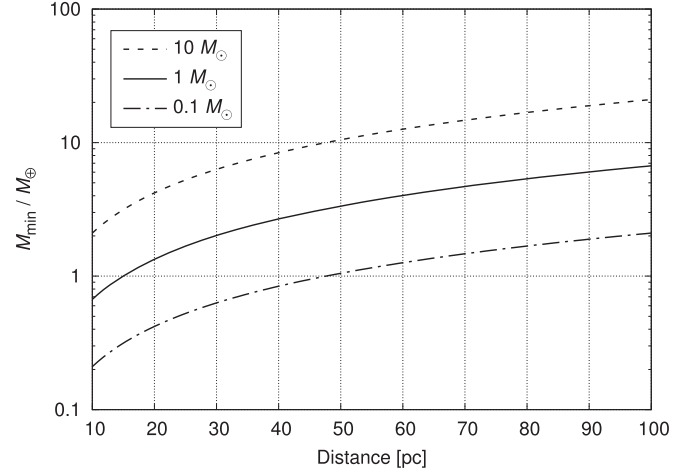


**Figure 4.** Minimum mass of detectable planet as a function of distance. The estimation assumes astrometric  $S/N = 3$ . The solid, dashed and dashed-dotted lines correspond to a solar-mass, upper- and lower-main sequence host star, respectively.

detectable for  $M_\star \lesssim 2.2 M_\odot$ , i.e., for A2V and later main-sequence star.

It is worth stressing that the detection limits refer to a mission lifetime of 5 yr, scaling as a function of such parameter.

#### 4.2. Pinpointing Exo-planets

We now briefly discuss how high-precision relative astrometry can be used for characterization of known exoplanetary systems. Many exoplanets have been discovered from radial velocity measurements. This technique can determine only the combination  $a_\star \sin i$ , where  $i$  is the orbit inclination. Accordingly, the planet mass is uncertain by the unknown factor  $\sin i$ .

In contrast, astrometry is capable of determining the inclination, together with the other Keplerian elements, and, therefore, it can provide valuable complementary information, allowing full characterization of planetary systems.

As an example, we consider HD147513b, a Jupiter mass planet orbiting a G3/G5V star with  $M = 0.92 M_\odot$  (Mayor et al. 2004). This system belongs to the Gaia primary sources, and its astrometric data have high accuracy, in particular the parallax relative error is  $\sigma_\varpi/\varpi = 8.5 \times 10^{-4}$ . The system characteristics are summarized in Table 1, deriving the astrometric parameters and radial velocity from the Gaia EDR3 (Gaia Collaboration et al. 2021) and DR2 (Gaia Collaboration 2018), respectively, while the orbital elements and the host star data are from the Extrasolar Planets Encyclopaedia.<sup>5</sup>

With parallax  $\varpi = 77.565$  mas, the distance to the system is 12.9 pc. Because of the inclination uncertainty, only the lower

<sup>5</sup> <http://exoplanet.eu/>

**Table 1**

Parameters of HD147513b (Gaia Source ID 6018047019138644480)

Parameter	Value	Uncertainty	Unit
$\alpha$	246.0058026652	0.057	deg; mas
$\delta$	-39.1929655698	0.038	deg; mas
$\varpi$	77.565	0.066	mas
$\mu_{\alpha*}$	73.748	0.082	mas yr <sup>-1</sup>
$\mu_{\delta}$	3.367	0.059	mas yr <sup>-1</sup>
$v_r$	12.889	0.132	km s <sup>-1</sup>
Apparent magnitude, $V$	5.37		mag
Mass, $M_p \sin i$	1.21		$M_J$
Semimajor axis, $a_p$	1.32		au
Orbital period, $P$	528.4	6.3	day
Eccentricity, $e$	0.26	0.05	
Argument of pericenter, $\omega$	282	9	deg
Pericenter passage epoch, $T_p$	2451672.0	11	JD

limit to the planet mass is known:  $M_p \gtrsim 1.21 M_J = 385 M_{\oplus}$ . This, in turn, results in an astrometric displacement due to the orbital motion at the level of at least  $130 \mu\text{as}$ .

In terms of our reference accuracy ( $0.2 \mu\text{as}$ ), this value is associated to an astrometric signal-to-noise ratio  $S/N \simeq 650$  (with maximum value of the inclination,  $i = 90^\circ$ ), or better with smaller inclination. A full astrometric solution, requiring several samples per orbit, can constrain the inclination, planetary mass and other parameters.

Figure 5 illustrates the apparent path of HD147513 on the celestial sphere, computed for the period from 2026 to 2031, using the data in Table 1. The trajectory shows a looping motion, i.e., the path intercepts itself several times at different times. It is clear from simple geometrical considerations that this happens when the parallax is larger than the annual proper motion, hence the feature is common to most nearby stars. The time distribution of the crossing events depends on the relationship between parallax and absolute value of proper motion  $\mu = (\mu_{\alpha*}^2 + \mu_{\delta}^2)^{-1/2}$ . For HD147513, with  $\varpi = 77.565$  mas and  $\mu = 73.825$  mas yr<sup>-1</sup>, the crossings are separated by 0.84, 1.29 and 1.62 yr.

The crossing points are favorable for planet discovery and orbit characterization by relative astrometry. Indeed, when a star returns to one such region, it fits in the same local frame, just slightly deformed due to proper motion and parallax of the reference (field) stars. Thus, repeated transits offer better opportunities to detect and measure the peculiarities of the target's motion, compared to other fields crossed just once by the star.

Therefore, the observation schedule can be optimized to take advantage of crossing conditions. The red dots in Figure 5 exemplify a distribution of observations with a uniform  $6$  point yr<sup>-1</sup> cadence, suited to conventional full astrometric solution, still approximately hitting eight of the twelve crossing points.

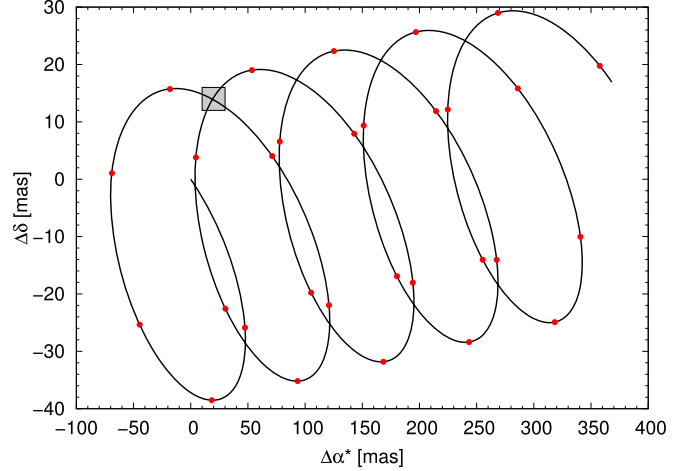


**Figure 5.** Path on the sky of HD147513, over 5 yr. The coordinates are reckoned from the starting position at J2026.0. The red dots give an example of observations sampled at the rate of 6 observation sets per a year. The shaded rectangle indicates the vicinity of a crossing point shown in Figure 6. The area size is greatly exaggerated in this drawing.

The fine structure of orbits close to a crossing point is further illustrated in Figure 6, where the stellar path is shown for three different values of inclination; the two visits are separated by a time elapse of 0.84 yr. Different inclinations imply different planet masses: the mass is minimum ( $1.21 M_J$ ) for an edge-on orbit with  $i = 90^\circ$ , while larger values are related to smaller inclinations:  $1.40 M_J$  for  $60^\circ$ , and  $2.42 M_J$  for  $30^\circ$ . The plot shows that, for the first passage, the green line is separated from the blue and red lines by about 1 and  $3 \mu\text{as}$ , respectively, and by some 50% less in the second transit. This difference is due to the changing orientation of the host star orbital position relative to the line-of-sight.

Using the same set of reference stars, differential astrometry is expected to localize the stellar path at sub- $\mu\text{as}$  precision. This, in turn, should make it possible to estimate the inclination to order of  $6^\circ$  ( $1\sigma$ ) in one crossing, because inclination affects the apparent stellar path.

This example evidences the relative astrometry capability to efficiently break the well-known degeneracy between planet mass and inclination, with few measurements. However, a full astrometric solution can provide all seven Keplerian elements, provided good enough observations (Perryman 2018). With its very high astrometric accuracy, therefore, RAFTER has a good potential for characterization of known planetary systems, for constraining planet masses as well as for improvement or independent determination of three-dimensional orbits.

## 5. Observations with an Annular Field

With respect to a conventional contiguous circular or rectangular field, an annular field observes at a given time several stars at some distance from a target (located within the

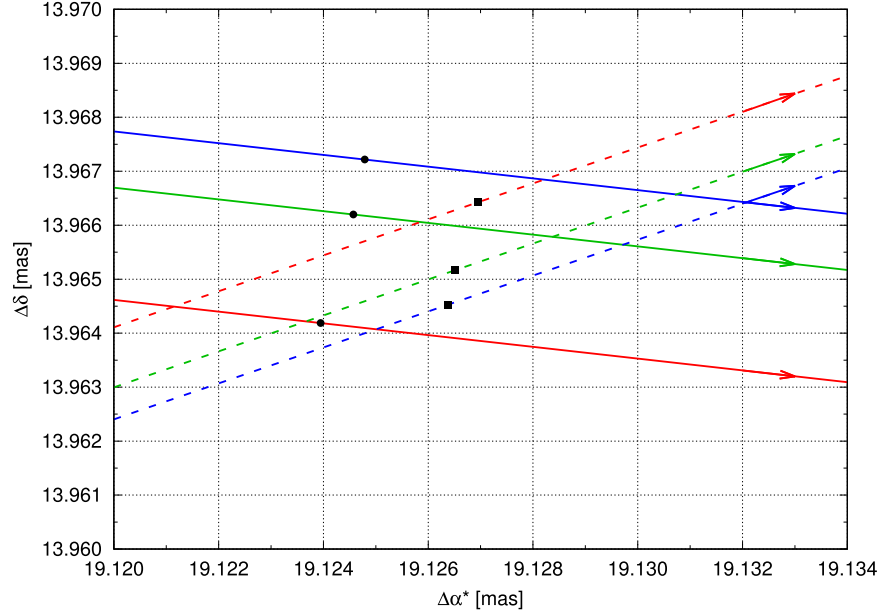


**Figure 6.** Zoomed view of the  $14 \times 10 \mu\text{as}$  area marked in Figure 5. The moments of observation when the star crosses the same area are separated by 0.84 yr. The red, blue and green lines show the path of the host star of the HD145513 system on the sky for inclination  $i = 30^\circ$ ,  $60^\circ$  and  $90^\circ$ , respectively. The first passage is drawn with the solid lines, while the dashed lines represent the second passage. The arrows indicate the direction of motion. The black dots illustrate positions of the star calculated at a fixed moment of time during the first passage. The black squares exemplify the same for the second passage.

focal plane ring populated by detectors), and does not “see” simultaneously many other nearby sources (inside the annulus). Such limitation can be overcome by a set of partially overlapped observations, as depicted in Figure 3. Some of the peculiar differences of annular and conventional contiguous field observations are evaluated below, by comparison of three cases:

1. A circular field with diameter  $0.5^\circ$ , comparable that proposed for Theia ( $\sim 0.2$  square deg);
2. A thin annular field with diameter  $2^\circ$  and width  $2'$ , radius  $58' \leq \rho \leq 1^\circ$ , with approximately the same area;
3. A thick annular field, width  $4'$  ( $56' \leq \rho \leq 1^\circ$ ), corresponding to RAFTER, with area  $\sim 0.4$  sq. deg.

With respect to the source HD147513b, described in Section 4.2, we have reference stars available in either case in significantly different magnitude ranges. In case 1, within  $0.5^\circ$  from the target, we have four stars, down to magnitude  $G = 10$  mag, as listed in Table 2. However, in cases 2 and 3, there are five stars within  $2^\circ$  distance brighter than  $G = 7$  mag, listed in Table 3. The annular field makes available brighter reference stars, with a gain of about 2 mag in this case. Such kind of evaluation is performed in our analysis to all bright targets ( $G \leq 8$  mag) in the sky, building up some relevant statistical results.

We select a sample of bright sources, and nearby reference stars, as described in Section 5.1. The main aspects considered

**Table 2**  
Reference Stars for HD147513b within  $0.5^\circ$ , Down to  $G = 10$  mag

Distance (deg)	$G$ (deg)	R.A. (deg)	Decl. (deg)
0.373	9.623	246.359	-38.941
0.390	8.728	246.321	-38.889
0.421	9.092	246.047	-38.773
0.439	8.812	246.539	-39.344

**Table 3**  
Reference Stars for HD147513b within  $2^\circ$ , Down to  $G = 7$  mag

Distance (deg)	$G$ (mag)	R.A. (deg)	Decl. (deg)
0.714	6.110	245.136	-39.431
0.851	6.621	245.061	-39.630
1.630	5.394	246.132	-37.566
1.777	6.408	245.781	-37.425
1.882	6.679	245.916	-41.074

in our analysis, based on the general considerations anticipated in Section 1, are:

1. the brightest accessible reference star (Section 5.2);
2. the number of available bright reference stars (Section 5.3);

3. the photon limited uncertainty on the position of the photocenter of the set of reference stars, against which the target is located (Section 5.4);
4. the uncertainty on target motion due to the limited knowledge on reference stars, i.e., the catalog induced errors (Section 5.5);
5. the potential improvement on the catalog data of the observed sample of reference stars achievable by exploitation of the new astrometric measurements (Section 5.6);
6. the benefits of a larger sample, achieved by setting a slightly fainter limiting magnitude for the reference stars (Section 5.7).

In our assessment, all the above aspects are considered independent of each other, for simplicity. In a practical case, observations should more appropriately be solved for both target and field stars, thus actually improving astrometry on all objects. Calibration is an intrinsic part of the process. The issue of such an “holistic” approach will be further investigated in future studies.

### 5.1. Sources from Gaia EDR3

The annular field performance is evaluated by simulation, using the Gaia EDR3 catalog for the astrometric parameters and magnitude of our star sample. The target stars are the 62,723 bright objects down to  $G = 8$  mag, whereas field stars are limited to  $G = 12$  mag (about three million objects) for most of the current exercise.

For each target, the field center is selected according to the criterion of including the brightest accessible partner star compatible with each case of focal plane geometry. The initial search is focused on a circular region with radius corresponding to the maximum detector size, as from Figure 1. In case 1, such radius is  $0.5^\circ$ , whereas in cases 2 and 3 it is  $2^\circ$ , thus providing access to a sky area 16 times larger (the ring width is mostly irrelevant).

The field of view is then placed according to the selected target-bright partner (BP) pair. In the central field case, the center is placed in the mid point of the line joining the pair, whereas in the annular cases the optical axis is displaced sufficiently to place both stars in the annulus, i.e., at  $1^\circ$  radius (see Figure 3). Further optimization of the observing region may depend on additional science requirements (e.g., including or avoiding specific field stars), but the subject is not addressed in the current simple framework. The total number of accessible field stars is listed in Table 4, together with some of the results of our analysis (described in the following).

### 5.2. Brightest Partner Matching Each Target

The field of view can be selected to include the target and the brightest accessible field star, hereafter Bright Partner (BP),

**Table 4**  
Statistics of the Stellar Sample; data from Gaia EDR3,  $G \leq 12$  mag

	Central	Annular 1	Annular 2
Total number of accessible field stars	1,310,469	1,380,708	2,683,834
Bright partner median magnitude (mag)	7.390	5.011	5.011
Bright partner rms magnitude (mag)	1.235	1.027	1.027
Individual bright partners	48,667	9,123	9,123
Median number of field stars, BP pointing	16	17	32
rms number of field stars, BP pointing	17.2	16.6	32.4
Median number of field stars, scan	59.0	233.5	467
rms number of field stars, scan	63.2	233.0	465.9
Field cumulative precision, median ( $\mu\text{as}$ )	0.224	0.155	0.143
Field cumulative precision, rms ( $\mu\text{as}$ )	0.112	0.106	0.064

considered as the most precise available astrometric reference thanks to its favourable photon budget.

For each target, the BP magnitude is brighter in the annular field cases (2 and 3) than for the central field by about two magnitudes, as shown in Figure 7. The number of BPs is larger than the number of stars at a given magnitude (left panel in figure), because several nearby targets are paired to a common reference bright star by the field selection strategy. Conversely, the central field case must resort to a larger number of fainter BPs in the close neighborhood of the target (right panel). This results in a higher sampling of bright stars over the set of measurements, used as BP to several fainter targets. The median and rms values of BP magnitude are listed in Table 4.

Due to the annular field’s definition, the same bright targets and BPs are selected in both cases 2 and 3.

### 5.3. Field Scan for more Reference Stars

An alternative observing strategy is considered, in order to evidence the annular field flexibility, consisting in selecting different fields for each target (by pointing offset, see Figure 1) throughout observations, thus piling up larger sets of reference stars. The two observing strategies will be referred to in the following as “BP pointing” and “scan”, respectively.

Releasing the requirement of simultaneous observation of target and BP, it is possible to point the instrument with more flexibility within the accessible area, thus increasing the number of observed field stars. E.g., we may assume three observations per year over five years (nominal mission lifetime), totalling 15 visits uniformly distributed in time, placed with a pointing offset such that the accessible region around each target is “scanned” in a roughly uniform way. This is beneficial e.g., in averaging down the catalog errors affecting the determination of each target’s motion, as discussed in Section 5.5.

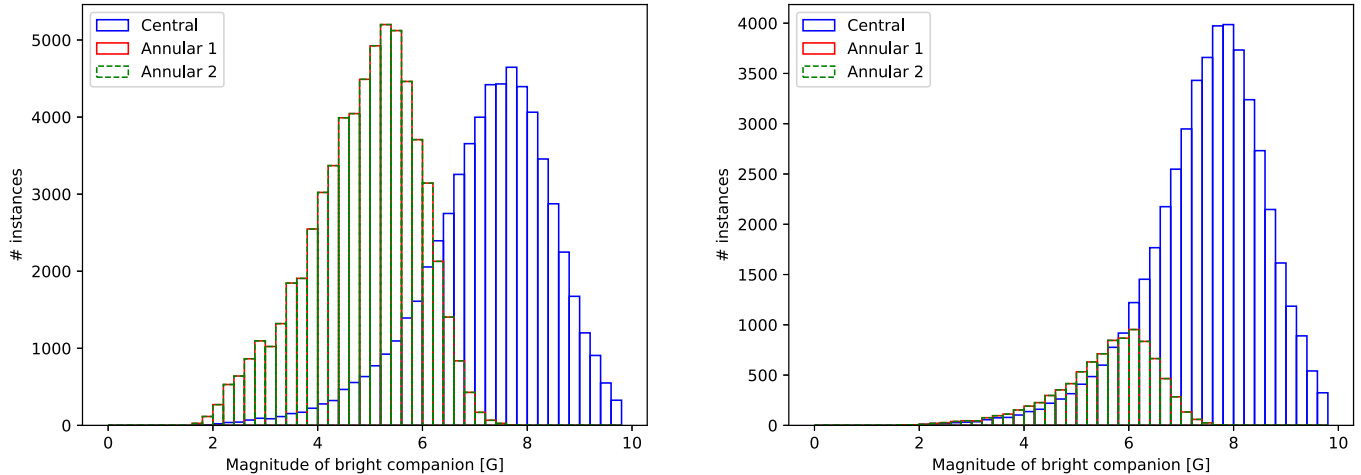


**Figure 7.** Bright partner magnitude: collective (one per target, left) and individual (duplicates removed, right).

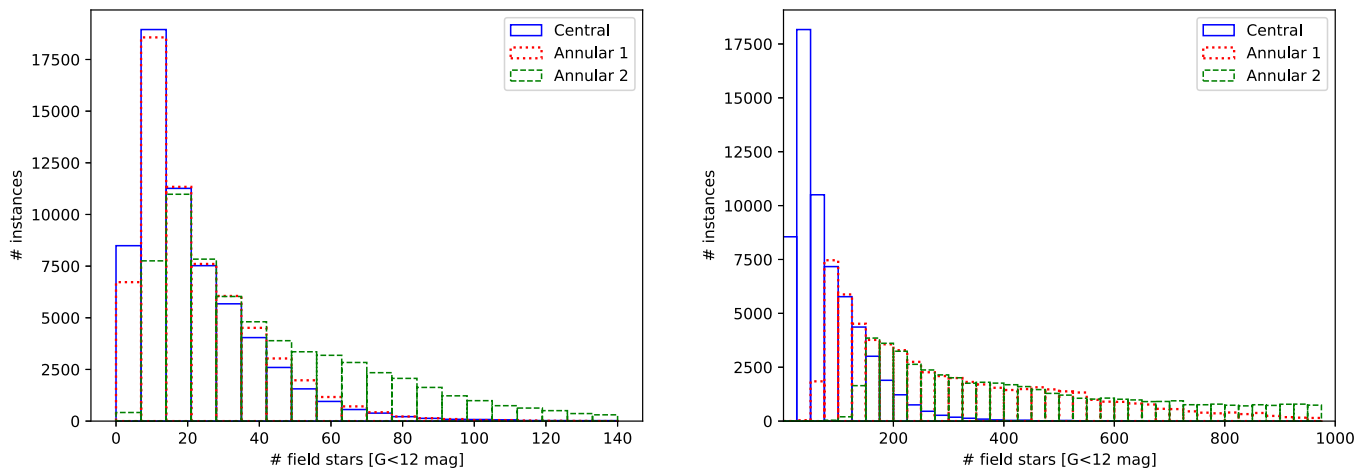


**Figure 8.** Histogram of field star population within  $G = 12$  mag, BP pointing (left) and field scan (right) observations.

The histogram of the number of field stars down to  $G = 12$  mag, for BP pointing, is shown in Figure 8 (left). Both central field and thin annular field cases provide comparable distributions (blue and red lines), according to their equal sky area coverage, with a median value of 16 and 17 reference stars, respectively, whereas the thick annular field case (green line) features a significantly larger number of field stars ( $>30$ ), thanks to its larger area.

Using multiple pointing offsets, 15 in our case, it is possible to accumulate observations over more field stars, within an accessible area which is larger for the annular than for the central field case. The resulting population of reference stars increases in any case, but the central field reaches a median star count  $\sim 60$ , against  $>230$  and  $>460$  respectively for the thin and thick annular field cases. The statistics is evidenced by the histograms in Figure 8 (right), and some of the resulting relevant figures are listed in Table 4.

#### 5.4. Photon Limited Uncertainty on Reference Frame

The field stars represent a materialization of the Gaia reference frame, providing a “grid” against which the target’s motion can be evaluated. The impact of catalog errors will be discussed in Section 5.5; here we just address the photon limited precision associated to the whole set of field stars selected for each target. For the current exercise, we assume BP pointing, with one hour exposure; the results from field scan are obviously expected to be even better, depending on implementation.

The target position with respect to the set of  $N$  field stars can be defined by its angular separation to each of them, whichever their actual current positions. The location uncertainties  $\sigma_n$ ,  $n = 1, \dots, N$  associated to each star’s magnitude is therefore combined by weighted average to provide the collective photocenter uncertainty  $\sigma_C$  (target excluded):

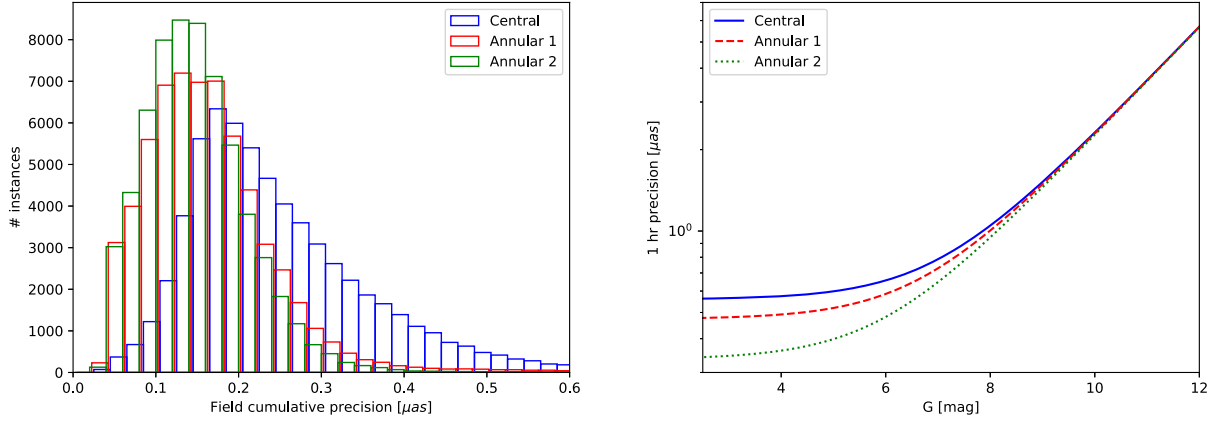


**Figure 9.** Cumulative field photocenter precision (left) and individual epoch precision, including field photocenter error (right).

$$\frac{1}{\sigma_C^2} = \sum_{n=1}^N \frac{1}{\sigma_n^2}. \quad (9)$$

This can be considered as the measurement precision of the reference frame in the current observation (single epoch).

For each target, the above collective uncertainty  $\sigma_C$  is computed, and its statistics is considered. The distribution of the results, shown in Figure 9 (left), is for most targets below  $1 \mu\text{as}$  for the central field case (blue line), and it improves progressively for the thin (red line) and thick (green line) annular field cases. The annular fields also evidence a more compact distribution, dominated by the higher precision of the lower magnitude BP.

The precision associated to individual observations is based on the photon limited precision (Mendez et al. 2014; Gai et al. 2017) for unresolved stars, diffraction limited images, and considering a 30% degradation factor from realistic instrument disturbances, for an exposure time of one hour per epoch. This is composed with a calibration error related to the field photocenter precision, choosing as a conservative value the median value of the distribution (Figure 9, left)  $+3\sigma$ , which includes  $>98\%$  of the cases. The resulting individual measurement uncertainty is shown in Figure 9 (right); the solid blue line refers to the central field, the dashed red line to the thin annular field, and the dotted green line to the thick annular field.

Assuming other error sources are kept at bay, sub- $\mu\text{as}$  precision is achieved for point-like sources brighter than  $G \simeq 8$  mag; the noise floor is therefore dominated by the field star statistics, and can be improved with observing strategy (e.g., field scan).

### 5.5. Catalogue Residual Errors

Repeated observations of our  $G \leq 8$  mag targets, to determine their dynamics, is affected by residual catalog errors from

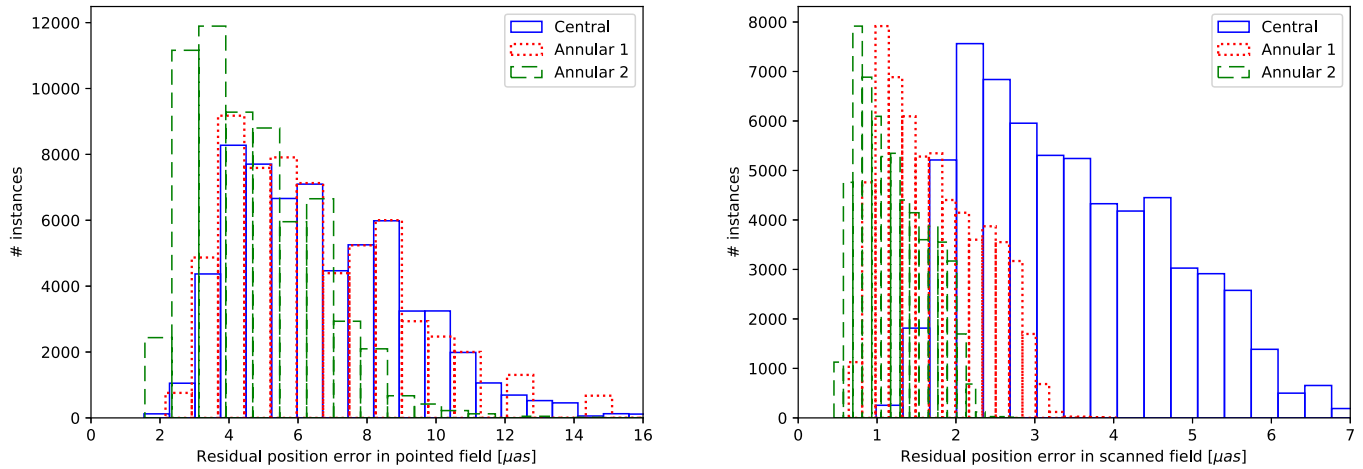
the set of field stars used as references, according to the preliminary remarks in Section 3.5. Such residual errors depend therefore on observing strategy, as suggested in Section 5.3: using different field stars will reduce the random component. The selected field star populations are those shown in Figure 8, respectively for fixed pointing (left), and for a set of 15 different pointing offsets (right).

The statistics from our simulation is shown in Figures 10, 11 and 12, respectively for position, proper motion and parallax. In the left panel, the results of repeated observation of the same field, i.e., using the same reference stars for each target, are shown. In the right panel, the values are related to the alternative field scan strategy, which selects different sets of field stars within the accessible area around the target (15 different pointing offsets throughout visits). In the latter case, the larger accessible sky area provided by the annular field makes available many more stars than the central field case, with a further improvement with the width of the annular field. Since each star is supposed to be affected by a random catalog error, the net effect is a more effective reduction of the overall uncertainty on the actual target position. Systematic catalog errors are supposed to be negligible.

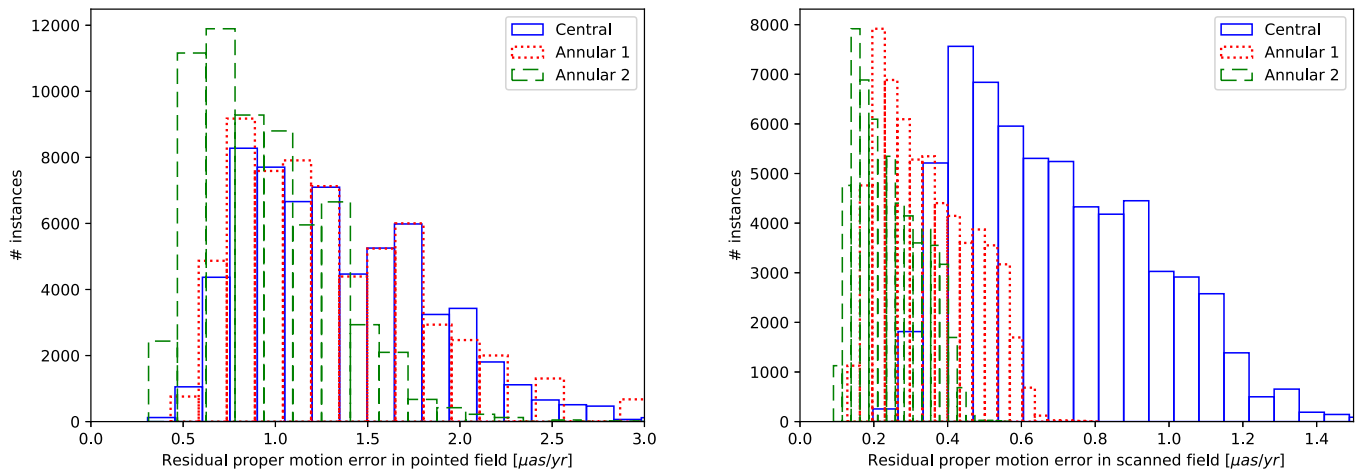
The results are in the range of a few  $\mu\text{as}$  on positions and parallaxes, and  $\sim 1 \mu\text{as yr}^{-1}$  on proper motion, just using a total observing time of 15 hr per target. This may be adequate to some science topic, but insufficient for others; however, smart tuning of the observing strategy appears able to provide impressive performance even with parsimonious usage of limited time resources. Relevant values are summarized in Table 5.

### 5.6. Catalogue Maintenance and Improvement

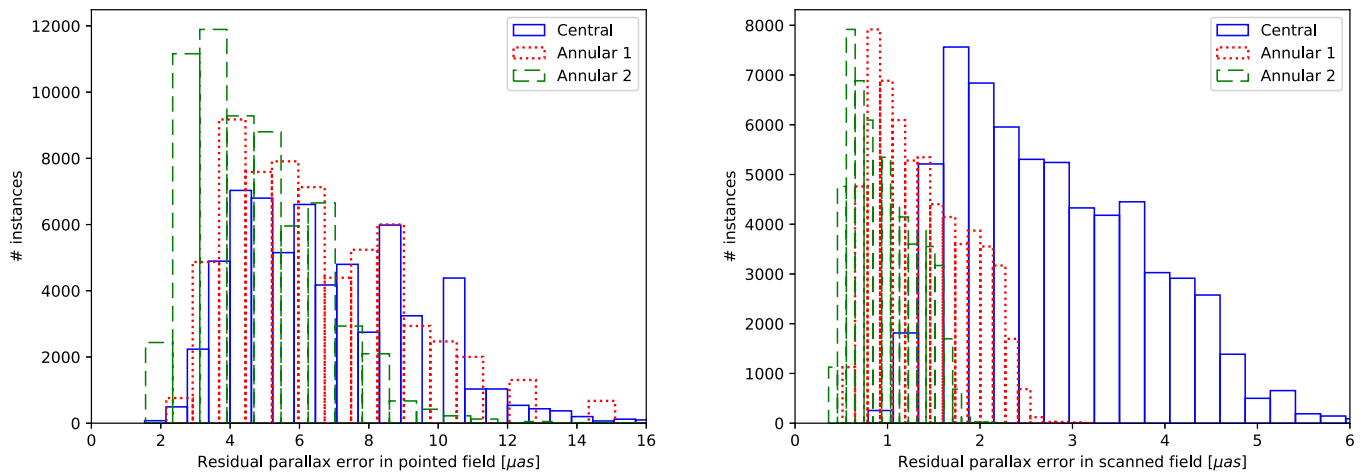
The astrometric measurements from observations may be used to improve, up to a point and in suitable conditions, the catalog precision on field stars, or at least to preserve it against



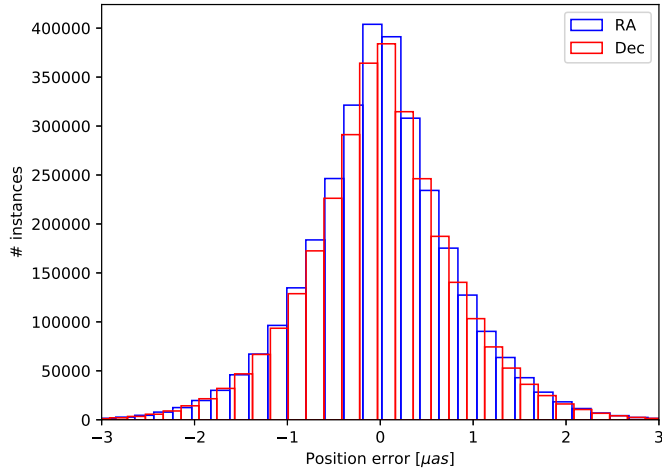
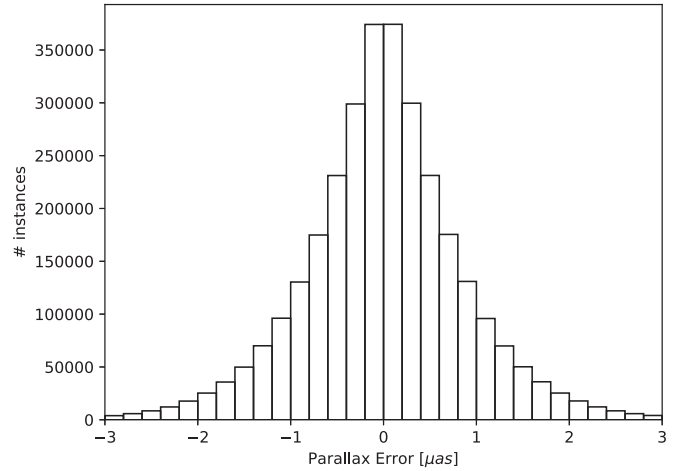
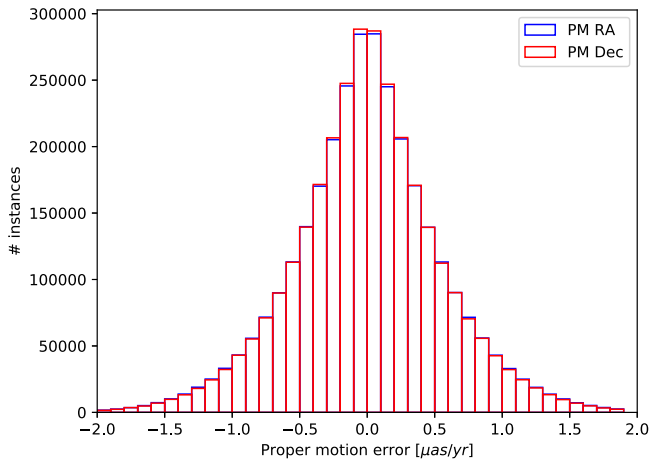
**Figure 10.** Catalogue limited position errors, single pointing (left) and with field scan strategy (right).



**Figure 11.** Catalogue limited proper motion errors, single pointing (left) and with field scan strategy (right).



**Figure 12.** Catalogue limited parallax errors, single pointing (left) and with field scan strategy (right).


**Figure 13.** Photon limited errors on reference star positions.

**Figure 15.** Photon limited errors on reference star parallaxes.

**Figure 14.** Photon limited errors on reference star proper motions.

**Table 5**  
Residual Catalogue Error

	Central	Annular 1	Annular 2
Median position, BP pointing ( $\mu\text{as}$ )	6.25	6.06	4.41
rms position, BP pointing ( $\mu\text{as}$ )	2.59	2.57	1.76
Median position, scan ( $\mu\text{as}$ )	3.25	1.64	1.16
rms position, scan ( $\mu\text{as}$ )	1.30	0.62	0.44
Median proper motion, BP pointing ( $\mu\text{as yr}^{-1}$ )	1.25	1.21	0.88
rms proper motion, BP pointing ( $\mu\text{as yr}^{-1}$ )	0.52	0.51	0.35
Median proper motion, scan ( $\mu\text{as yr}^{-1}$ )	0.65	0.33	0.23
rms proper motion, scan ( $\mu\text{as yr}^{-1}$ )	0.26	0.12	0.09
Median parallax, BP pointing ( $\mu\text{as}$ )	6.25	6.07	4.41
rms parallax, BP pointing ( $\mu\text{as}$ )	2.58	2.57	1.75
Median parallax, scan ( $\mu\text{as}$ )	2.60	1.31	0.93
rms parallax, scan ( $\mu\text{as}$ )	1.04	0.49	0.35

**Table 6**  
Astrometric Catalogue Bootstrap by Observation of Field Star

	Central	Annular 1	Annular 2
Median position error ( $\mu\text{as}$ )	3.25	1.64	1.16
rms position error ( $\mu\text{as}$ )	1.30	0.62	0.44
Median proper motion error ( $\mu\text{as yr}^{-1}$ )	0.65	0.33	0.23
rms proper motion error ( $\mu\text{as yr}^{-1}$ )	0.26	0.12	0.09
Median parallax error ( $\mu\text{as}$ )	2.60	1.31	0.93
rms parallax error ( $\mu\text{as}$ )	1.04	0.49	0.35

natural degradation. Not only field star errors can be averaged out effectively to get proper determination of any target's kinematic parameters, but in principle astrometry on field stars can be improved as well, assuming they are observed repeatedly throughout the mission lifetime. We again assume three observations per year over five years, uniformly distributed. This simulation is performed on the whole sample of Gaia objects down to  $G=12$  mag, each considered as a single star with a simple linear motion described by the five astrometric parameters in the catalog. Each star is located against the reference system materialised by the set of remaining objects, using the single epoch precision in Figure 9 (right).

The full sample provides a realistic distribution of positions on the sky, proper motion and parallax, suited to our immediate goal of evaluating the potential improvement on astrometric parameters of field stars achievable with the proposed observing strategy. In practice, depending on target and sampling scheme selection from the main science case, the number of field star subject to astrometric bootstrap may range, e.g., between few ten thousand to few hundred thousand objects.

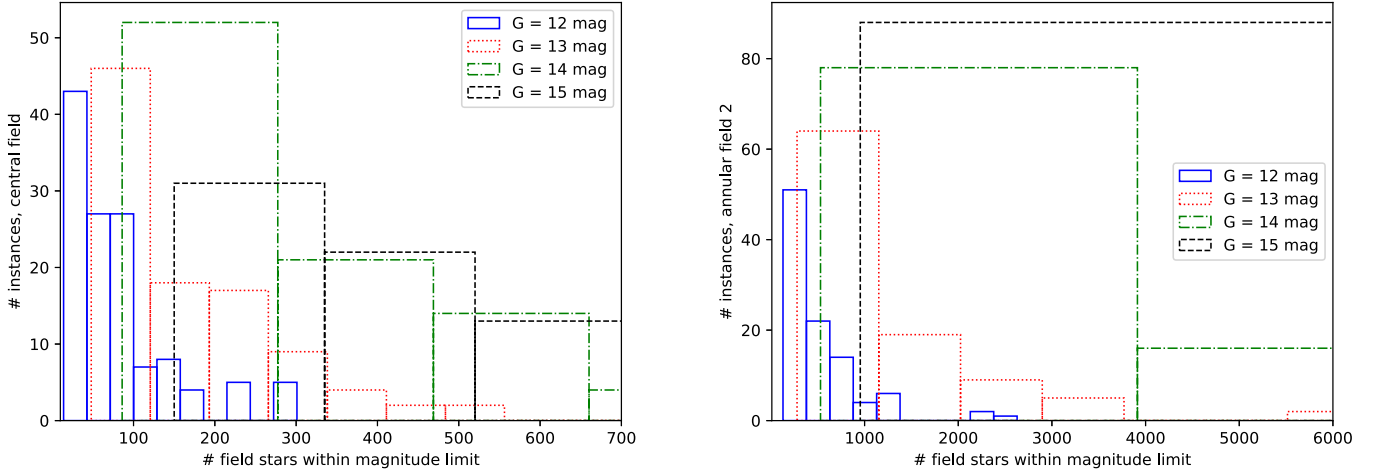


**Figure 16.** Number of field stars as a function of the limiting magnitude, for the central (left) and thick annular field (right).

**Table 7**  
Number of Field Stars as a Function of Magnitude

$G$ mag	Central		Thin Annular		Thick Annular	
	Median	rms	Median	rms	Median	rms
12	59.0	70.9	185.5	220.6	371.0	441.1
13	124.0	134.9	400.8	659.7	801.5	1,319.4
14	258.5	458.9	880.9	2,082.4	1,761.8	4,164.8
15	483.0	1,491.3	1,903.6	6,404.5	3,807.2	12,808.9

The results of the simulation are shown in Figures 13, 14 and 15, respectively for positions, proper motions and parallaxes. The corresponding statistics (median errors and their rms spread) is reported in Table 6; median errors improve from the central, through the thin annular, to the thick annular field case. The rms of experimental errors may be considered as an expectation on the variability expected among different fields, depending mainly on source density. The estimation does not include the residual catalog (absolute) errors, i.e., it is strictly relative astrometry.

### 5.7. Pushing Toward Fainter Magnitude

Most of the evaluations in previous sections have been performed on a slice of the Gaia EDR3 catalog limited to  $G \leq 12$  mag, for reasons of practicality. The number of available field stars obviously increases by setting a fainter limiting magnitude. It may be noted that fainter stars, e.g., down to  $G \leq 15$  mag, are still quite bright for a 1 m class telescope, requiring elementary exposure time below 1 minute, and providing an epoch location uncertainty of  $\lesssim 10 \mu\text{s}$  in one hour. It may be expected that, in general, random error components on the reference frame materialization (implemented by the whole set of field stars) will improve by setting a

fainter limiting magnitude, i.e., using more stars, albeit each affected by comparably large individual errors.

The star density in the range  $12 \leq G \leq 15$  mag is more dependent on Galactic latitude, compared to brighter sources, which are somewhat more uniformly distributed. A simple assessment of average sky density has been performed by selecting from the Gaia catalog a sample of all sources over the range  $G \leq 12$  mag, within a  $2^\circ$  radius around 100 bright objects in the range  $4.2 \lesssim G \lesssim 6$  mag, distributed on rather sparse positions on the sky.

The number of stars down to a given magnitude in this sample is shown in Figure 16, respectively for the central (left) and thick annular (right) case. The thin annular case, intermediate between the others, is omitted for the sake of brevity. The typical number of reference stars increases with the limiting magnitude, and it is significantly larger in the latter case, as expected. Statistical values are listed in Table 7; the large spread evidenced by the rms is mainly due to the variation in star population with Galactic latitude.

## 6. Conclusions


The potential for relative astrometry of a 1 m class space telescope endowed with an annular field of view with  $\sim 1^\circ$  radius is evaluated by comparison with a conventional instrument concept with a compact focal plane detector. Basic concepts of astrometry as a tool for crucial parameter determination are recalled, in particular with respect to real mass determination of exo-planetary systems. We evidence that smart observing plans, exploiting prior knowledge on individual targets, result in efficient measurement, e.g., pinpointing orbit inclinations, and therefore true planet masses, with a minimum number of dedicated observations. The statistics on reference field stars brighter than  $G = 12$  mag, for targets down to  $G = 8$  mag, is evaluated on the Gaia EDR3 catalog; the

potential of sufficiently wide sets of Gaia sources as local materialization of the reference frame at the  $\mu\text{as}$  level is discussed. The annular field provides the capability of finding adequate reference objects to a larger distance from the selected target than the central field, thus improving on the overall astrometric measurement because more and/or brighter field stars are made available. In particular, in our scenario, each target may find in the annular field individual reference stars typically 2 mag brighter than in the central field, or many more stars (four to seven times as many in the example described), resulting in a more reliable reference frame. Repeated observation of selected sources (several ten thousand, to a few hundred thousand) may “refresh” their astrometric parameters, mitigating the natural catalog degradation with time.

The activity has been partially funded by a grant from the Italian Ministry of Foreign Affairs and International Cooperation (ASTRA: Astrometric Science and Technology Roadmap), and by the Italian Space Agency (ASI) under contract 2018-24-HH.0.

### ORCID iDs

M. Gai,  <https://orcid.org/0000-0001-9008-134X>

A. Vecchiato  <https://orcid.org/0000-0003-1399-5556>

M. G. Lattanzi  <https://orcid.org/0000-0003-0429-7748>

### References

- Banik, I., & Kroupa, P. 2019, *MNRAS*, **487**, 1653  
 Bendek, E., Tuthill, P., Guyon, O., et al. 2018, *Proc. SPIE*, **10698**, 106980G  
 Boden, A. F., Shao, M., & Van Buren, D. 1998, *ApJ*, **502**, 538

- Borucki, W. J., & Summers, A. L. 1984, *Icarus*, **58**, 121  
 Butkevich, A. G. 2018, *MNRAS*, **476**, 5658  
 Casewell, S. L., Belardi, C., Parsons, S. G., et al. 2020, *MNRAS*, **497**, 3571  
 Charpinet, S., Fontaine, G., Brassard, P., et al. 2011, *Natur*, **480**, 496  
 Contigiani, O., Rossi, E. M., & Marchetti, T. 2019, *MNRAS*, **487**, 4025  
 Coronado, J., Rix, H.-W., & Trick, W. H. 2018, *MNRAS*, **481**, 2970  
 Croft, R. A. C. 2021, *MNRAS*, **501**, 2688  
 Damasso, M., Sozzetti, A., Lovis, C., et al. 2020, *A&A*, **642**, A31  
 Gai, M., Busonero, D., & Cancelliere, R. 2017, *PASP*, **129**, 054502  
 Gaia Collaboration 2018, *yCat*, **1/345**  
 Gaia Collaboration, Brown, A. G. A., Vallenari, A., et al. 2021, *A&A*, **649**, A1  
 Gould, A., & Chanamé, J. 2004, *ApJS*, **150**, 455  
 Jedamzik, K. 2020, *JCAP*, **2020**, 022  
 Kervella, P., Arenou, F., Mignard, F., & Thévenin, F. 2019, *A&A*, **623**, A72  
 Korsch, D. 1977, *ApOpt*, **16**, 2074  
 Lindegren, L., Klioner, S. A., Hernández, J., et al. 2021, *A&A*, **649**, A2  
 Lu, J. R., Sinukoff, E., Ofek, E. O., Udalski, A., & Kozłowski, S. 2016, *ApJ*, **830**, 41  
 Malbet, F., Boehm, C., Krone-Martins, A., et al. 2021, *ExA*, **51**, 845  
 Marchetti, T., Contigiani, O., Rossi, E. M., et al. 2018, *MNRAS*, **476**, 4697  
 Marchetti, T., Rossi, E. M., Kordopatis, G., et al. 2017, *MNRAS*, **470**, 1388  
 Mayor, M., Udry, S., Naef, D., et al. 2004, *A&A*, **415**, 391  
 Mendez, R. A., Silva, J. F., Orosz, R., & Lobos, R. 2014, *PASP*, **126**, 798  
 Miller-Jones, J. C. A., Bahramian, A., Orosz, J. A., et al. 2021, *Sci*, **371**, 1046  
 Pasquale, B., Content, D., Kruk, J., et al. 2014, *Proc. SPIE*, **9293**, 929305  
 Perryman, M. 2018, *The Exoplanet Handbook* (Cambridge: Cambridge Univ. Press)  
 Perryman, M., Hartman, J., Bakos, G. A. †, & Lindegren, L. 2014, *ApJ*, **797**, 14  
 Prusti, T., De Bruijne, J., Brown, A., et al. 2016, *A&A*, **595**, A1  
 Quinn, D. P., Wilkinson, M. I., Irwin, M. J., et al. 2010, in *ASP Conf. Ser.* **435**, Binaries—Key to Comprehension of the Universe, ed. A. Prša & M. Zejda (San Francisco, CA: ASP), 453  
 Ranalli, P., Hobbs, D., & Lindegren, L. 2018, *A&A*, **614**, A30  
 Rappaport, S., Levine, A., Chiang, E., et al. 2012, *ApJ*, **752**, 1  
 Riva, A., Gai, M., Vecchiato, A., et al. 2020, *Proc. SPIE*, **11443**, 114430P  
 Rybicki, K. A., Wyrzykowski, L., Bachelet, E., et al. 2022, *A&A*, **657**, A18  
 Shao, M., Turyshev, S. G., Zhai, C., et al. 2019, *BAAS*, **51**, 74  
 Sozzetti, A., Giacobbe, P., Lattanzi, M. G., et al. 2014, *MNRAS*, **437**, 497  
 Tian, H.-J., El-Badry, K., Rix, H.-W., & Gould, A. 2020, *ApJS*, **246**, 4  
 Tuthill, P., Bendek, E., Guyon, O., et al. 2018, *Proc. SPIE*, **10701**, 107011J  
 Wheeler, J. C., & Johnson, V. 2011, *ApJ*, **738**, 163  
 Yoo, J., Chanamé, J., & Gould, A. 2004, *ApJ*, **601**, 311  
 Zhai, C., Shao, M., Goullioud, R., & Nemati, B. 2011, *RSPSA*, **467**, 3550